Spatially resolved study of the dynamics of Josephson tunnel junctions

S. G. Lachenmann, T. Doderer, R. P. Huebener, and D. Quenter
Physikalisches Institut, Lehrstuhl Experimentalphysik II, Universität Tübingen, W-7400 Tübingen, Germany

J. Niemeyer and R. Pöpel
Physikalisch-Technische Bundesanstalt, W-3300 Braunschweig, Germany
(Received 30 November 1992; revised manuscript received 13 April 1993)

By scanning superconducting $Nb/Al_2O_3/Nb$ tunnel junctions of various geometries with an electron beam at low temperatures we have obtained spatially resolved two-dimensional images related with the dynamics of the junctions. In a current-biased junction the local thermal perturbation effected by the beam results in a voltage change ΔV representing a convenient imaging-response signal. The spatial resolution is limited by a characteristic thermal healing length with a value of about 2 μm in our experiments. We analyze our results in terms of the sine-Gordon equation. For the interpretation of the spatially resolved voltage signal ΔV we extend the energetic analysis of the perturbed sine-Gordon system of McLaughlin and Scott by including the beam-induced local thermal perturbation. Our model allows the quantitative comparison of our experimental two-dimensional images with the local dynamics expected from the perturbed sine-Gordon equation. Our experiments include the observation of single-mode and multiple-mode cavity resonances, soliton oscillations, and flux-flow behavior.

I. INTRODUCTION

Following the discovery of the Josephson effects 30 years ago,[1] the static and dynamic properties of Josephson junctions have been extensively investigated experimentally and theoretically.[2,3] Experimentally mostly only global junction properties have been studied such as the current voltage characteristic (IVC) or specific high-frequency properties of the junction. In addition to these global measurements spatially resolved experiments have been reported for Josephson tunnel junctions using electron-beam scanning[4–6] or laser-beam scanning[7] of the junction area. These spatially resolved measurements were restricted mostly to the static states of the junction and two papers dealt specifically with the dynamic state.[8,9]

The dynamics of Josephson tunnel junctions is well described by a model based on the perturbed sine-Gordon equation (PSGE) together with the appropriate boundary conditions. In this dynamics we can distinguish between the following two limiting regimes. For large-area junctions, where the boundary conditions only play a minor role, we encounter solitons moving across the junction. On the other hand, if the boundary conditions become more dominant, as, for example, for small junction dimensions, the soliton character of the solution of the PSGE is lost and replaced by electromagnetic resonant cavity modes. However, in both regimes the various excitations display distinct temporal and spatial structures.

In this paper we report spatially resolved measurements of a large variety of different complex dynamic excitations of Josephson tunnel junctions using low-temperature scanning electron microscopy (LTSEM) for two-dimensional imaging. Our experiments include multiple-mode oscillations, soliton oscillations, and flux-flow behavior. For the interpretation of the spatially resolved LTSEM signal we have developed a model based on the energetic analysis of the perturbed sine-Gordon system of McLaughlin and Scott.[10] This model allows the quantitative comparison of our experimental two-dimensional images with calculations based on approximate solutions of the PSGE. The present paper represents an important extension of our previous imaging studies of one- and two-dimensional Fiske modes.[8] Preliminary results have been reported elsewhere.[11]

II. ELECTRODYNAMICS OF JOSEPHSON TUNNEL JUNCTIONS AND LTSEM SIGNAL GENERATION

A. Electrodynamics

The electrodynamics of Josephson tunnel junctions is governed by the PSGE

$$\Phi_{xx}+\Phi_{yy}-\Phi_{tt}-\sin\Phi=\alpha\Phi_t-\beta(\Phi_{xxt}+\Phi_{yyt}) \quad (1)$$

for the phase difference Φ between the superconducting junction electrodes.[2,3] Here the barrier plane is identical with the x-y plane. The indices denote the partial derivatives with respect to the indicated variables. The spatial coordinates x and y and time t are normalized to the Josephson penetration depth λ_J and to the inverse of the Josephson plasma frequency, $1/\omega_p$, respectively. The loss term $\alpha\Phi_t$ describes the quasiparticle tunneling losses and the term $\beta(\Phi_{xxt}+\Phi_{yyt})$ the surface losses. The length and width of the junction are denoted by l and w, respectively. The corresponding normalized distances are $L=l/\lambda_J$ and $W=w/\lambda_J$. The boundary conditions at the boundaries $x=0,L$ and $y=0,W$ are defined from the x and y components of the external magnetic field and from the electric current applied to the junction.

Depending on the junction geometry, Eq. (1) can be

simplified. Since most of our experiments were restricted to the *in-line geometry*,[2] we concentrate on this case. For this the bias current only flows near the junction edges and is treated usually only in terms of the boundary conditions. With the current flow in the x direction we have

$$\Phi_{xx}-\Phi_{tt}-\sin\Phi=\alpha\Phi_t-\beta\Phi_{xxt} \tag{2}$$

with the boundary conditions

$$\begin{aligned}&\Phi_x(0,t)+\beta\Phi_{xt}(0,t)=-\kappa+\eta\ ,\\&\Phi_x(L,t)+\beta\Phi_{xt}(L,t)=\kappa+\eta\ .\end{aligned} \tag{3}$$

Here $\eta=H_y/J_0\lambda_J$ is the external magnetic field, and $\kappa=I_B/2J_0w\lambda_J$ takes into account the bias current. J_0 is the critical Josephson current density.

For describing the dynamic dissipative states of the tunnel junction two theoretical approaches have been developed in the past. The perturbation theory by McLaughlin and Scott[10] starts with the analytic soliton solutions of the unperturbed sine-Gordon equation ($\alpha=\beta=0$) and treats the damping coefficients α and β as small perturbations. They restricted their treatment to the one-dimensional case. This approach can be used for either L or $W\gg1$, weak boundary conditions, and small perturbations. However, for increasing perturbation and/or influence of the boundary conditions the solutions of the PSGE are expected to deviate more and more from the pure soliton solutions. If the junction dimensions become sufficiently small or the magnetic field sufficiently large, the localized soliton solutions change into electromagnetic waves in the form of cavity resonance modes.[2] In the limit of small junction dimensions and/or high magnetic fields the dynamics can be described by a single mode. This single-mode approach has been developed by Takanaka for zero-field steps[12] and by Kulik for Fiske steps.[13] A natural extension of this approach is the multiple-mode theory proposed by Enpuku, Yoshida, and Irie[14] in which the solutions of the PSGE are approximated by a spatial Fourier expansion.

Of course, between the two limiting regimes discussed above, namely, the solitonlike treatment and the multiple-mode expansion, solutions of the PSGE can be obtained by standard numerical techniques.

B. Electron beam scanning and response signal

A spatially resolved study of the dynamics in Josephson tunnel junctions is possible in a straightforward way by scanning the junction area with an electron beam and by recording a suitable response signal while the junction is operated in the particular dynamic state to be investigated. This technique of LTSEM is described in detail elsewhere.[15–18] Here we only emphasize the following essential points. The junction is scanned with the electron beam of a scanning electron microscope, while the bottom of the substrate carrying the junction is in intimate thermal contact with liquid He. The electron beam acts as a local heat source, causing a thermal perturbation of the sample near the coordinate point (x_0,y_0) of the beam focus. The lateral dimension of this thermal perturbation limits the spatial resolution of the LTSEM imaging technique. As an example for junction electrodes from Nb with a total thickness of 0.5–1 μm this limit is typically 1–3 μm. Typical values for the voltage and current of the beam are 25–35 kV and 10–100 pA, respectively, yielding a total local temperature increment of 0.1–1 K. For a current-biased junction operation the beam-induced voltage change $\Delta V(x_0,y_0)$ represents a convenient response signal for two-dimensional imaging. [Of course, the beam-induced current change $\Delta I(x_0,y_0)$ would be another suitable response signal if the junction is operated under voltage bias.]

In the following we construct a model for relating the voltage signal $\Delta V(x_0,y_0)$ to the local dynamics of the junction at the coordinate point (x_0,y_0) of the electron-beam focus. For this purpose the energetic analysis of the perturbed sine-Gordon system performed by McLaughlin and Scott[10] provides a highly promising path to follow.

For simplicity we consider an infinitely long one-dimensional junction extending along the x coordinate. The unperturbed sine-Gordon equation

$$\Phi_{xx}-\Phi_{tt}-\sin\Phi=0 \tag{4}$$

describes a Hamiltonian system.[10] On the other hand, for a real in-line junction of finite length L the energy input is affected by the boundary conditions expressed in (3). The temporal change of the total energy can be calculated according to[19]

$$\begin{aligned}\frac{dH}{dt}=&\int_0^L(-\alpha\Phi_t^2-\beta\Phi_{xt}^2)dx+\eta\Phi_t(L)-\eta\Phi_t(0)\\&+\kappa\Phi_t(L)+\kappa\Phi_t(0)\ .\end{aligned} \tag{5}$$

The dissipative α and β terms extract energy from the sine-Gordon system, whereas the external magnetic field (described by η) reduces the energy at the junction edge $x=0$ and increases the energy at the edge $y=L$. The bias current provides energy input at both junction edges.

The local thermal perturbation of the tunnel junction by the electron-beam irradiation results in a change of the energy balance discussed above. The primary effect of the local heating due to the electron beam is expected to be a local increment $\Delta\alpha(x_0)$ and $\Delta\beta(x_0)$ of the damping coefficients α and β, respectively, which is assumed to be independent of x_0 for homogeneous junctions. For simplicity, we neglect the spatial extension of the perturbed area for our calculations. Operating the junctions at low temperature ($T\approx4$ K) and considering a small temperature increment of less than 1 K, we may neglect the influence of the e-beam irradiation on the critical-current density and on the London penetration depths of the junction electrodes in a first approximation. If the bias-current I_B is kept constant during the scanning experiments, in the case of moving solitons it is immediately obvious that they will be slowed down, resulting in a reduction of the junction voltage by $\Delta V(x_0)$. Note, if the local reduction of the critical-current density would dominate the junction response signal, we expect an increase of the junction voltage[8] in contradiction to our experimental observations.

For any further discussion it is important to look at the

different time scales involved in the electron-beam scanning process. The beam irradiation time for an individual image point on the sample surface is typically 10^{-3} s. On the other hand, the typical thermal relaxation time of the local region perturbed by the beam is about 10^{-7} s.[15,16] However, the dynamics in the tunnel junction is much faster. The imaging experiments are usually performed with an operating voltage on the IVC of a sample of 10 μV or larger, yielding a time scale of the junction dynamics of 10^{-10} s or smaller. Hence, the response signal $\Delta V(x_0)$ must be obtained from the time-averaged equations.

The typical relative magnitude of the response signal is $|\Delta V/V| \approx 10^{-3}-10^{-4}$. Therefore, the signal can be found in good approximation from a linearized treatment. We can see from (5) that if we would express the beam-induced additional damping described by the increments $\Delta\alpha(x_0)$ and $\Delta\beta(x_0)$ in terms of an effective reduction $\Delta I_{\rm eff}(x_0)$ of the driving current, we can write the voltage signal as

$$\Delta V(x_0)=\frac{\partial V}{\partial I}(I_B)\Delta I_{\rm eff}(x_0) \ . \tag{6}$$

In the limit where linearization is appropriate, $\partial V/\partial I$ in (6) is the differential resistance of the unirradiated junction. From (6) we note the expected result that the response signal $|\Delta V(x_0)|$ increases proportional to the derivative $\partial V/\partial I(I_B)$ of the IVC of the junction.

The time-averaged electron-beam-induced power losses are, according to Eq. (5),

$$\left\langle \frac{d\Delta H}{dt} \right\rangle = -\Delta\alpha\langle \Phi_t^2 \rangle - \Delta\beta\langle \Phi_{xt}^2 \rangle \ , \tag{7}$$

where $\langle\ \rangle$ denotes the time average. For small changes $\Delta\alpha/\alpha$ and $\Delta\beta/\beta$ we expect a linear relation between the response signal $\Delta V(x_0)$ and the power loss of Eq. (7) and, hence, the proportionality:

$$\Delta V(x_0) \sim -\Delta\alpha\langle [\Phi_t(x_0)]^2 \rangle - \Delta\beta\langle [\Phi_{xt}(x_0)]^2 \rangle \ . \tag{8}$$

In Eqs. (7) and (8) we have neglected the first-order contribution arising from the beam-induced change $\Delta\Phi$ of the phase difference function $\Phi(x,t)$. As we can see from the close correspondence of our experimental results shown in the following with our calculations neglecting an e-beam-induced change of Φ, this approximation seems to be appropriate. However, an accurate mathematical evaluation of this approximation still needs to be done.

From Eq. (8) we see that the contributions of $\Delta\alpha$ and $\Delta\beta$ to the voltage signal are modulated by the time average of the square of the local electric field $\langle [\phi_t(x_0)]^2 \rangle$ and of the square of the local time derivative of the magnetic field $\langle [\phi_{xt}(x_0)]^2 \rangle$ in the junction, respectively. Equation (8) represents the main result of our energetic analysis of the perturbed sine-Gordon system for obtaining a theoretical expression for the LTSEM response signal $\Delta V(x_0)$ for comparison with experiments. In the following sections we perform such a comparison for a variety of dissipative dynamic states, concentrating on the two limiting regimes of one- and two-dimensional multiple-mode and soliton behavior.

III. CAVITY MODES DESCRIBED BY MULTIMODE EXPANSION

A. Multimode expansion

For solving the PSGE (2) in the one-dimensional case with the boundary conditions (3) Enpuku, Yoshida, and Irie[14] expanded Φ in terms of a sum of spatial Fourier modes with time-dependent amplitudes. This formalism can be extended to two dimensions in a straightforward way. So far in the literature it appears that only single-mode excitations have been discussed for two dimensions. A tunnel junction of width W and length L is described by the two-dimensional PSGE (1) under the boundary conditions which represent an extension of those given in Ref. 20:

$$\begin{aligned}
&\Phi_x(0,y,t)+\beta[\Phi_{xt}(0,y,t)+\Phi_{yt}(0,y,t)]=\eta_y+\tilde{\kappa} \ , \\
&\Phi_x(L,y,t)+\beta[\Phi_{xt}(L,y,t)+\Phi_{yt}(L,y,t)]=\eta_y \ , \\
&\Phi_y(x,0,t)+\beta[\Phi_{xt}(x,0,t)+\Phi_{yt}(x,0,t)]=-\eta_x+\tilde{\kappa} \ , \\
&\Phi_y(x,W,t)+\beta[\Phi_{xt}(x,W,t)+\Phi_{yt}(x,W,t)]=-\eta_x \ .
\end{aligned} \tag{9}$$

$\tilde{\kappa}=I_B/2J_0wl$ denotes the bias current, $\eta_x=H_x/\lambda_J J_0$ the x component, and $\eta_y=H_y/\lambda_J J_0$ the y component of the external magnetic field. The expansion

$$\Phi(x,y,t)=\omega_0' t-\eta_x y+\eta_y x-\frac{\tilde{\kappa}}{2L}(x-L)^2-\frac{\tilde{\kappa}}{2W}(y-W)^2 + \sum_{n,m=0}^{\infty} \Theta_{n,m}(t)\cos(nk_{r,x}' x)\cos(mk_{r,y}' y) \tag{10}$$

with $k_{r,x}'=\pi/L$, $k_{r,y}'=\pi/W$, and $\omega_0'=\omega_0/\omega_p$ satisfies the boundary conditions. In the resonance case the Josephson frequency ω_0 corresponds to a cavity mode[21]

$$\omega_{n,m}=\bar{c}\pi\left[\left[\frac{n}{1}\right]^2+\left[\frac{m}{w}\right]^2\right]^{1/2} \ , \tag{11}$$

where $\bar{c}$ is the Swihart velocity. Analogous to the one-dimensional case[14] we use the approximation

$$\Theta_{n,m}^r = A_{n,m}\cdot\cos(\omega_{n,m}'\cdot t+\phi_{n,m}) \tag{12}$$

with $\omega_{n,m}'=\omega_{n,m}/\omega_p$. Here $A_{n,m}$ and $\phi_{n,m}$ denote the amplitude and phase, respectively, of the particular mode. Similar to the one-dimensional case[14] we expect that the amplitudes $A_{n,m}$ decrease with increasing n and m. For the resonance case (11) we then obtain for the LTSEM voltage signal

$$-\Delta V(x_0,y_0)\sim\Delta\alpha\left[\omega_0'^2+\tfrac{1}{2}\sum_{n,m}\omega_{n,m}'^2 A_{n,m}^2\cos^2(nk_{r,x}'x)\cos^2(mk_{r,y}'y)\right]$$
$$+\Delta\beta\left[\tfrac{1}{2}\sum_{n,m}\omega_{n,m}'^2 n^2 k_{r,x}'^2 A_{n,m}^2\sin^2(nk_{r,x}'x)\cos^2(mk_{r,y}'y)\right]$$
$$+\Delta\beta\left[\tfrac{1}{2}\sum_{n,m}\omega_{n,m}'^2 m^2 k_{r,y}'^2 A_{n,m}^2\cos^2(nk_{r,x}'x)\sin^2(mk_{r,y}'y)\right]. \quad (13)$$

The range of validity of the multiple-mode expansion is determined by the following parameters: the geometrical size of the tunneling window (in units of λ_J), the barrier-parallel applied magnetic field, the number of the studied resonance step. In a barrier-parallel magnetic-field Fiske steps appear in the IVC. For a rectangular junction of length l and width w the steps are observed at the voltages[21]

$$V_{n,m}^{\text{Fiske}}=\frac{h\bar{c}}{4e}\left[\left[\frac{n}{l}\right]^2+\left[\frac{m}{w}\right]^2\right]^{1/2}, \quad (14)$$

where m and n are integers. If the magnetic field is oriented parallel to one junction edge, we expect one-dimensional Fiske modes, otherwise two-dimensional Fiske modes. For zero magnetic field, zero-field steps are generated. Extending the one-dimensional excitations discussed in the literature[12,22,23] to two dimensions, we expect for the voltage levels at the zero-field steps

$$V_{n,m}^{\text{ZFS}}=\frac{h\bar{c}}{2e}\left[\left[\frac{n}{l}\right]^2+\left[\frac{m}{w}\right]^2\right]^{1/2}, \quad (15)$$

i.e., twice the value of the corresponding Fiske step. Whether one- or two-dimensional modes are excited depends upon the geometric configuration of the current leads and upon preferential directions given by the junction geometry.

B. LTSEM imaging: Regime of cavity modes

Following our earlier imaging studies of one- and two-dimensional Fiske modes,[8] in the present investigation we have imaged nearly all one- and two-dimensional Fiske modes up to the (12,12) mode with a square junction of cross-type geometry.[2] As an example we show in Fig. 1 the (10,0) *Fiske mode* for a $Nb/Al_2O_3/Nb$ tunnel junction with 140×140 μm^2 area ($\lambda_J=40$ μm). The result in Fig. 1 illustrates that for the nth Fiske mode only the nth Fourier mode is significantly excited. These states can be well described by the single-mode theory of Kulik.[13] Taking only the nth term of the sum in Eq. (13) and setting $m=0$, one obtains a homogeneous and a modulated part, in agreement with Fig. 1. Whether the modulated part represents the time average of the square of the magnetic component (with zero amplitude at the junction edges) or of the electric component (with maximum amplitude at the junction edges) of the Fiske mode depends upon $\Delta\alpha$, $\Delta\beta$, the step number, and the length of the junction. However, in our experiments we have always observed a dominating magnetic component.

Figure 2 shows the first and second one-dimensional *zero-field step* for a cross-type $Nb/Al_2O_3/Nb$ junction

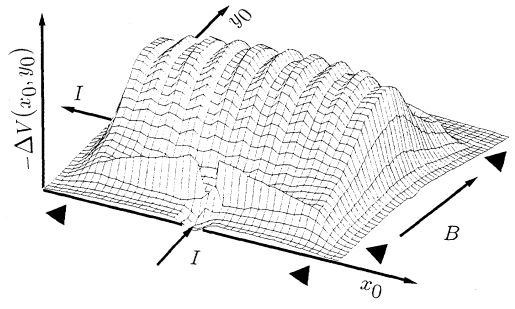

FIG. 1. Voltage image $-\Delta V(x_0,y_0)$ of the (10,0) Fiske mode. Junction dimension 140×140 μm^2 ($\lambda_J=40$ μm). The junction edges are indicated by the arrows. The magnetic field (0.4 mT) is oriented parallel to the junction edge along the y direction. $T\approx4$ K.

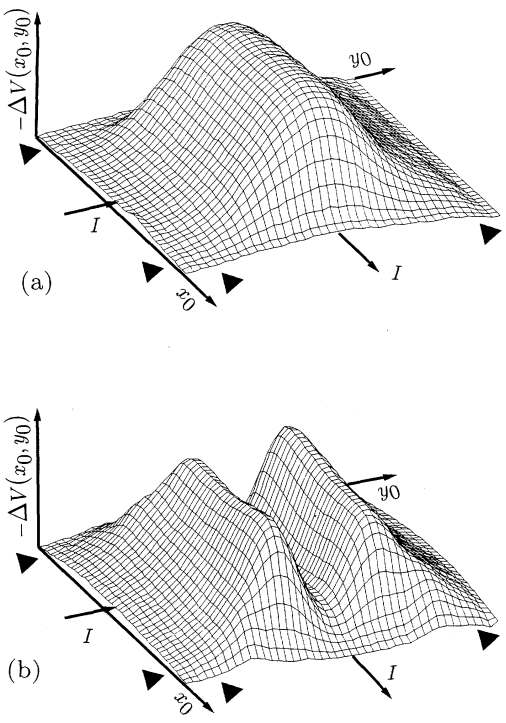

FIG. 2. Voltage image $-\Delta V(x_0)$ of the first (a) and second (b) one-dimensional zero-field step. The geometry of the current flow is shown. Junction dimension 50×50 μm^2 ($\lambda_J=25$ μm). The junction edges are indicated by the arrows. $T\approx4$ K.

with a 50×50 μm^2 area ($\lambda_J=25$ μm). The geometry of the current flow is also indicated. We see that for the first zero-field step only the mode with frequency $\omega_1=\omega_{0,1}$ is predominantly excited, whereas for the second zero-field step the mode with frequency $\omega_2=\omega_{0,2}=2\omega_{0,1}$ is dominant. From Fig. 2 one can further deduce that the resonance frequency ω_r of the cavity is given by $\omega_r=0.5\omega_0$, where ω_0 is the Josephson frequency of the voltage step. Hence, the data in Fig. 2 confirm the theory of Takanaka regarding zero-field steps in small tunnel junctions.[12]

For larger tunnel junctions the single-mode expansion is not adequate anymore. As an example we show in Fig. 3 the voltage images of the first three zero-field steps of an in-line $Nb/Al_2O_3/Nb$ junction of 124 μm (3.5 λ_J) length and 20 μm width (with superconducting ground plane). The second and third zero-field steps are seen to display only a significant excitation of the frequency $\omega_{2,0}$ and $\omega_{3,0}$, respectively. On the other hand, in the first zero-field step several modes are excited simultaneously. For comparison, in Fig. 3(d) we show a theoretical voltage image of the first zero-field step calculated from Eq. (13) using the ratio

$$A_{2,0}^2\left[4\Delta\beta\frac{\pi^2}{L^2}-\Delta\alpha\right]\Big/A_{1,0}^2\left[\Delta\beta\frac{\pi^2}{L^2}-\Delta\alpha\right]=0.15$$

and setting $A_{n,0}=0$ for $n>2$. We see that the calculated curve agrees reasonably with the experimental result of Fig. 3(a).

Two examples of voltage images observed for *two-dimensional Fiske modes* are shown in Fig 4, namely, the (1,3) mode in Fig. 4(a) and the (1,7) mode in Fig. 4(c). The geometry of the current flow and the magnetic-field orientation are indicated in Figs. 4(a) and 4(c). The sample is the same as in Fig. 1. For comparison in Fig. 4(b) we show the theoretical voltage image calculated from Eq. (13) assuming a single-mode excitation for the mode

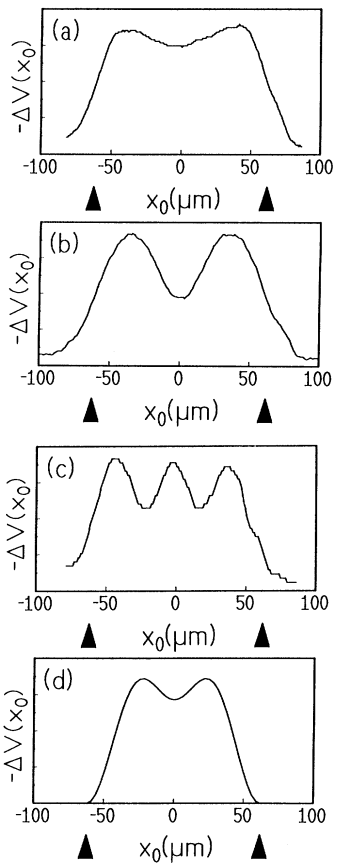

FIG. 3. Voltage image $-\Delta V(x_0)$ of the first (a), second (b), and third (c) zero-field step of an in-line junction with 124 μm length and 20 μm width with superconducting ground plane ($\lambda_J=35$ μm). The junction edges are indicated by the arrows. $T\approx4$ K. (d) shows a theoretical curve $-\Delta V(x_0)$ calculated from Eq. (13) as specified in the text.

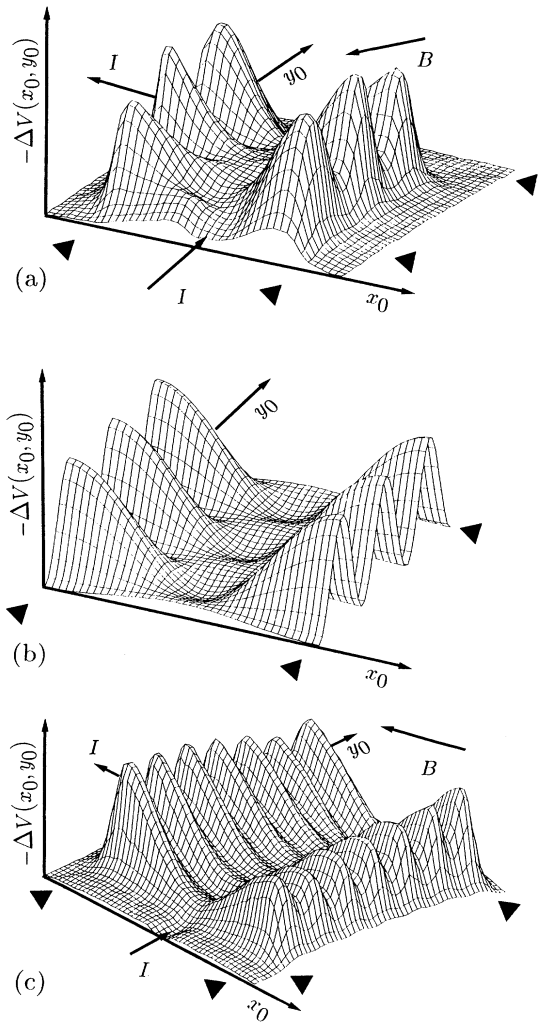

FIG. 4. Voltage images $-\Delta V(x_0,y_0)$ of the two-dimensional Fiske modes (1,3) in (a) and (1,7) in (c). The sample is the same as in Fig. 1. The geometry of the current flow and the magnetic-field orientation is indicated. $T\approx4$ K. (b) shows the voltage image calculated from Eq. (13) for the mode numbers $n=1$ and $m=3$. The junction edges are indicated by the arrows.

numbers $n=1$ and $m=3$. In this calculation for simplicity we have neglected the electron-beam-induced change $\Delta\alpha$. We note satisfactory agreement between experiment and theory.

Finally, in Fig. 5 we show the voltage image of the first diagonal Fiske mode for the same sample as in Figs. 1 and 4 [Figs. 5(a) and 5(b)] and of the first diagonal zero-field mode for the same sample as in Fig. 2 [Fig. 5(c)]. Figure 5(a) displays the experimental result, whereas Fig. 5(b) contains the theoretical image calculated from Eq. (13) for the (1,1) Fiske mode. Apparently, in this case a significant contribution of the higher harmonic $\omega_{2,2}$ is needed to reproduce the experimental result. The calculation was performed using the ratio $A_{2,2}^2/A_{1,1}^2=0.035$ and setting all nondiagonal and higher harmonic amplitudes equal to zero. Again, for simplicity we have neglected $\Delta\alpha$. Figure 5(c) displays the experimental voltage image of the first diagonal zero-field mode. This mode can be well accounted for theoretically using $A_{2,2}^2/A_{1,1}^2=0.015$ and setting all other amplitudes equal to zero as above for the first diagonal Fiske mode.

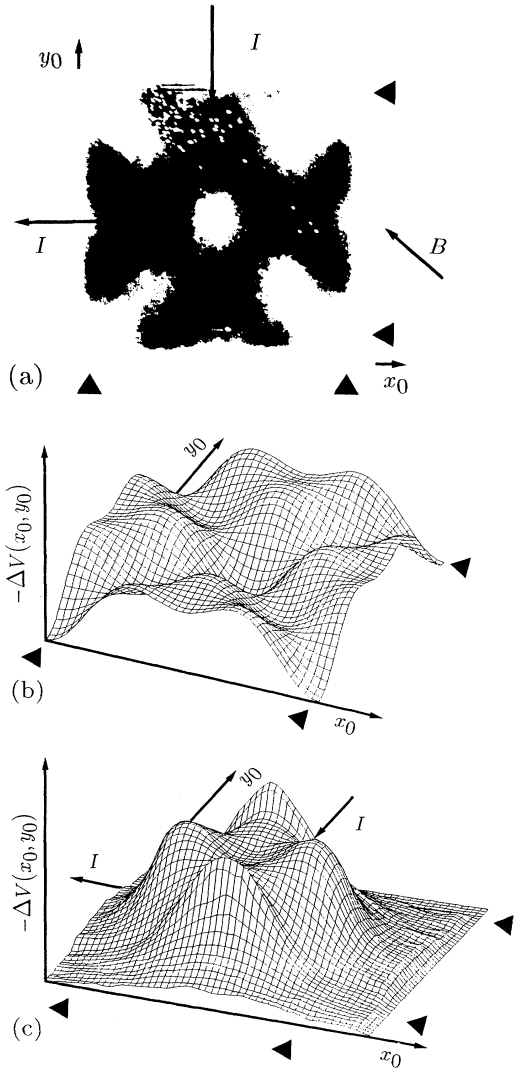

FIG. 5. Voltage image $-\Delta V(x_0,y_0)$ of the (1,1) Fiske mode (a) shown in brightness modulation (dark regions indicate large signals $|\Delta V|$) and theoretical voltage image (b) calculated from Eq. (13). Same sample as in Figs. 1 and 4. (c) Voltage image of the first diagonal zero-field mode for the same sample as in Fig. 2. $T\approx 4$ K. The junction edges are indicated by the arrows.

Our spatially resolved measurements have confirmed that three parameters determine the number of modes needed for describing the dynamic state of the junction: the junction size in units of λ_J, the applied magnetic field, and the step number. This behavior is in agreement with the theory and numerical simulations. If the boundary conditions become dominating for the dynamics of the tunnel junction, the characteristic nonlinearity of the sine-Gordon system cannot develop, and the states can be described using linear approximations. The boundary conditions become more dominant the smaller the junction size, the higher the external magnetic field, and the larger the order number of the resonance step investigated.

In the opposite limit of large junctions the multiple-mode expansion is less promising. Here the dynamics of the junction can be described better in terms of approximations based on the solutions of the pure sine-Gordon equation, i.e., in terms of solitons. We turn to this soliton dynamics in the next section.

IV. SOLITON DYNAMICS IN JOSEPHSON JUNCTIONS

A. LTSEM voltage signal

A theoretical treatment of the voltage signal generated by a local perturbation of the tunnel junction has been reported by Chang.[24] He used a perturbation technique for solving the PSGE. In contrast to the approach by Chang, in the following we treat the LTSEM voltage signal in terms of simple physical arguments providing a more direct insight into the problem. Our arguments are based on the perturbed energy balance discussed by McLaughlin and Scott.[10]

The time-dependent velocity $u(t)$ of the perturbed sine-Gordon soliton is governed by the following nonlinear differential equation for the velocity $u(t)$:[10]

$$\frac{du}{dt}=-\alpha u(1-u^2)-\tfrac{1}{3}\beta u \ . \tag{16}$$

u is normalized to the Swihart velocity $\bar{c}$ and runs between -1 and $+1$. This equation refers to the in-line geometry. The energy input at both junction edges is provided by the bias current. The α and β terms cause damping of the vortices.

Again we take the local increment of the damping parameters α and β by the amount $\Delta\alpha$ and $\Delta\beta$, respectively, as the dominating effect of the electron-beam irradiation. As a result, the soliton velocity is reduced. The analytic solution of Eq. (16) is given by

$$u(t)=(c_1e^{2bt}+d)^{-1/2} \tag{17}$$

with $c_1=(1/u_0^2)-(\alpha/b)$, $b=\alpha+(\beta/3)$, $d=\alpha/b$. u_0 denotes the starting velocity at $t=0$. If the coordinate point x_0 is irradiated by the beam, the soliton has the ve-

locity $u(t)$ of Eq. (17) until it reaches the region around x_0. In this perturbed region the velocity is reduced to

$$u_1(t)=(c_2e^{2bt+z}+d_1)^{-1/2} . \tag{18}$$

Here $z=2\Delta b\cdot\Delta t$ indicates the damping increment Δb multiplied with the time interval Δt in which the beam-induced perturbation is felt by the moving soliton. After passing the perturbation, the soliton moves on with unchanged damping. Since both the α and β terms show a similar effect, namely, decelerating the soliton, for simplicity in the following calculation we only consider the effective change of the α term.

The first zero-field step is due to the periodic motion of a single soliton. The spatial dependence of the unperturbed soliton velocity is found from Eq. (17) yielding

$$u(x)=\frac{e^{-2\alpha x}(u_0+1)+(u_0-1)}{e^{-2\alpha x}(u_0+1)-(u_0-1)} \tag{19}$$

with $u(0)=u_0$. A typical velocity profile for an in-line junction of length $11\lambda_J$ is shown in Fig. 6(a). The dashed curve represents the soliton velocity without electron-beam irradiation obtained from Eq. (19), whereas the solid curve indicates the velocity for beam irradiation at the coordinate $x_0=3$. Note that both curves only differ from each other in the region where the soliton moves away from the irradiation point x_0. For calculating the curves in Fig. 6(a) realistic parameter values have been used: $\alpha=0.027$ (obtained from the IVC with the help of Ref. 25), $u_0=0.95$ [found from the time-averaged velocity $\langle u\rangle$ and the velocity profile of Eq. (19); $\langle u\rangle$ was obtained from the measured voltage at the bias current],

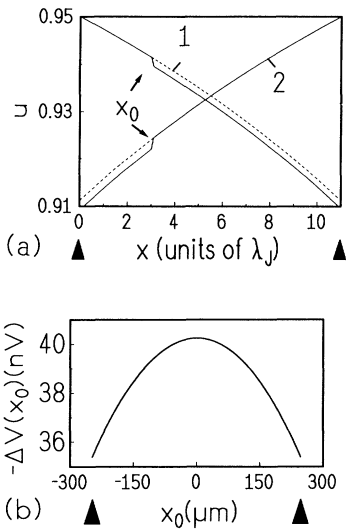

FIG. 6. (a) Typical soliton velocity profile for an in-line junction of length $11\lambda_J$. u is normalized to the Swihart velocity $\bar{c}$ and is measured in normalized units. The solid curve shows the velocity for beam irradiation at the coordinate $x_0=3\lambda_J$. The dashed curve refers to zero beam irradiation. (b) Voltage signal $-\Delta V(x_0)$ expected from the beam-induced change of the average soliton velocity $\langle u\rangle$ calculated analytically with the same parameters as in Fig. 6.

and $z=0.03$ (estimated from the magnitude of the observed voltage signal ΔV).

Since the soliton velocity is not constant, the beam-induced change of $\langle u\rangle$ and thereby the voltage signal ΔV depends upon the coordinate x_0 of the irradiation point. By integration over the perturbed velocity profile the voltage signal ΔV can be calculated analytically[26] and is plotted in Fig. 6(b). In conjunction with this signal ΔV we note the following. If the starting velocity u_0 is the same at both ends of the junction, ΔV displays a maximum in the middle. If the starting velocity is different at both ends, the maximum shifts to the side with the higher starting velocity. With increasing damping coefficient α the maximum in the middle becomes more pronounced.

So far we have neglected the effects arising when the solitons collide with the edges of the junction. This collision process is discussed in detail in Refs. 25 and 27. From these results the beam perturbation is expected to cause the additional energy loss in the collision zone

$$\Delta H_{\rm coll}=-2\pi^2\Delta\alpha f(u) . \tag{20}$$

Extending the argument of Ref. 25, this energy loss can be expressed in terms of a reduction of the bias current by the amount $(\pi/2)\Delta\alpha f(u)$. Using the analytic function between the bias current and the time-averaged junction voltage given in Ref. 25, again we obtain an expression for the voltage signal proportional to $\Delta\alpha$. This represents an additional contribution to the voltage signal for all locations where soliton collisions take place.

Whereas for zero applied magnetic field the voltage signal is generally expected to display the same symmetry as the sample configuration, in the presence of a *barrier-parallel external magnetic field* this symmetry of the voltage signal is broken, of course. For the beam-induced voltage signal we now expect qualitatively the following nonsymmetric behavior. We restrict our discussion to flux flow steps, i.e., to sufficiently high magnetic fields, where the flux quanta always move through the junction in a single direction. In the limit of weak coupling between the fluxons in the junction the beam irradiation only decelerates the individual fluxons after they have passed the location of the beam focus. The resulting reduction of the time-averaged fluxon velocity will be larger the closer to the nucleation site of the soliton the beam focus is located. Hence, we expect a voltage signal $|\Delta V|$ decreasing monotonically from the soliton point of entry to the point of exit. However, in addition to this effect the *e*-beam irradiation will specifically influence the nucleation process of the fluxons. From this, we also expect a reduction of the voltage signal as the coordinate point of the beam focus moves away from the nucleation site. On the other hand, in the limit of rigid coupling between the fluxons the effect of the beam irradiation and the signal $|\Delta V|$ will be constant along the direction of the soliton motion.

B. LTSEM imaging: Regime of soliton modes

In the following we present a few selected typical results illustrating both the soliton dynamics in large Josephson junctions and confirming the LTSEM signal

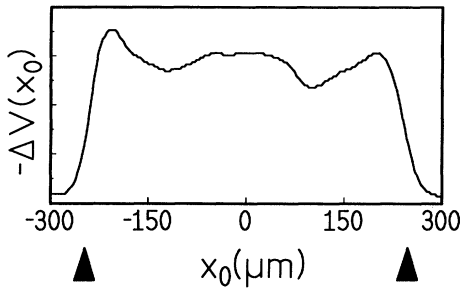

FIG. 7. Voltage image $-\Delta V(x_0)$ of the first zero-field step of a one-dimensional in-line junction of 494 μm length and 30 μm width ($\lambda_J = 45$ μm; line scan along the long dimension). $T \approx 4$ K. The junction edges are indicated by the arrows.

generating mechanism discussed in the last section for spatially resolved investigation of this dynamics.

Figure 7 shows the voltage image of the first zero-field step of a long one-dimensional in-line $Nb/Al_2O_3/Nb$ junction of 494 μm length ($11\lambda_J$) and 30 μm width (line scan along the long junction dimension). The junction configuration had a ground plane. The nonsymmetry of the bias current flow due to the ground plane was compensated by means of a small barrier-parallel magnetic field of 0.036 mT. The results of Fig. 7 confirm the behavior expected from our discussion in Sec. IV A. The maximum in the middle of the junction and the two maxima in the collision zones near both edges can clearly be seen. The following additional observations also agree with the theoretical expectations. Increasing the electron-beam power results in a larger signal $|\Delta V|$ and the maxima become more pronounced as expected from the larger increment $\Delta\alpha$. If the sample temperature is reduced, the damping coefficient α and its beam-induced increment $\Delta\alpha$ become smaller, yielding a reduced magnitude of the voltage signal, as observed experimentally. Finally, shifting the bias point upward on the IVC, the signals become smaller as expected [see Eq. (6)].

Two voltage images of the second zero-field step recorded for the same junction as in Fig. 7 are shown in Fig. 8. The second zero-field step is associated with two solitons moving simultaneously through the junction. The line scan in Fig. 8(a) was obtained at low bias current. Its main features consist of three maxima which are indicated by arrows. These maxima can be qualitatively explained in terms of soliton-antisoliton collision peaks associated with a symmetric soliton mode,[28,29] where in each half of the junction a single soliton is moving. In addition to the collision peaks near the junction edges we then expect one more collision peak in the middle of the junction.

Figure 8(b) shows the signal for the same junction obtained at high-bias current. Now all maxima except for the two near the junction edges have disappeared. We observed a change of the voltage image from the behavior of Fig. 8(a) to that of Fig. 8(b) by increasing the bias current and vice versa. This result can be explained in terms of the bunching effect expected for high-bias currents and, hence, high soliton velocities where the two solitons move closely together through the junction, and where collision peaks can be generated only near both junction edges. So far, such bunching effects have been discussed only in overlap[28,29] and in annular[30] junctions.

Two images of flux-flow steps can be seen in Fig. 9 for the same junction as in Fig. 7. In Fig. 9(a), the barrier-parallel magnetic field was 0.61 mT, corresponding to

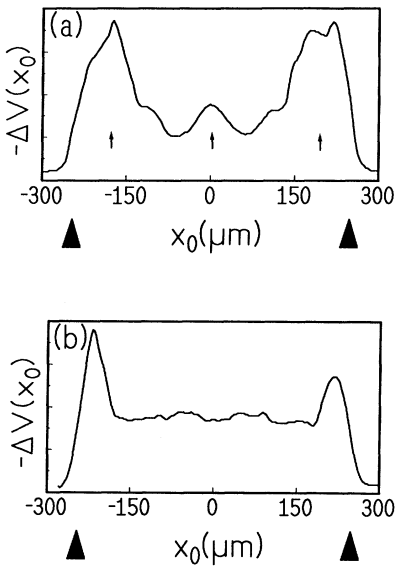

FIG. 8. Voltage image $-\Delta V(x_0)$ of the second zero-field step of the same in-line junction as in Fig. 7 (line scan along the long dimension) at low-bias current, $\kappa = 0.28$ (a) and high-bias current, $\kappa = 0.44$ (b). $T \approx 4$ K. The junction edges are indicated by the arrows.

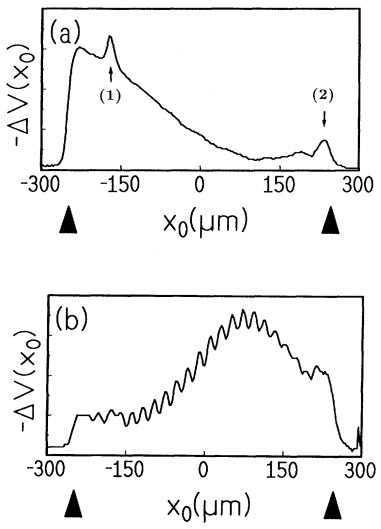

FIG. 9. Voltage image $-\Delta V(x_0)$ for the same in-line junction as in Fig. 7 for a barrier-parallel magnetic field of 0.61 mT (a) and 0.29 mT (b). The small signal peaks marked (1) and (2) in (a) are due to a local microshort and a small overlap region of the junction counter electrode with the wiring layer, respectively. $T \approx 4$ K. The junction edges are indicated by the arrows.

25.4 flux quanta in the junction, and the fluxons move from left to right. In Fig. 9(b) the magnetic field was 0.29 mT, corresponding to 12 flux quanta in the junction, and the fluxons move from right to left. The result of Fig. 9(a) confirms our expectation discussed above for weak coupling between the fluxons that the signal $|\Delta V|$ decreases monotonically from the entry to the exit point of the fluxons. Compared to Fig. 9(a), in Fig. 9(b) the magnetic field and the voltage was about half in magnitude. The voltage in Fig. 9(b) corresponds to the 24th Fiske step, as expected from 12 flux quanta in the junction.[2] In the sample shown in Figs. 7–9 we have observed Fiske behavior only in the form of an additional structure superimposed on the voltage signal $\Delta V(x_0)$ associated with flux-flow behavior. In Fig. 9(b) we note 24 superimposed small oscillations. Apparently, in this case the dynamics of the junction is characterized by the superposition of the resonance motion of the fluxons (Fiske behavior due to reflection at the junction edges) and the flux-flow behavior.[31]

ACKNOWLEDGMENTS

Financial support of this work by a grant of the Deutsche Forschungsgemeinschaft is gratefully acknowledged. F. Hebrank and S. Lemke generously supplied a series of specimens and assisted during some of the measurements. The authors would like to thank T. Weimann, P. T. B. Braunschweig for his help during the sample fabrication, and M. Koyanagi, ETL, Ibaraki, Japan and R. Gross for manufacturing some of the samples.

[1]B. D. Josephson, Phys. Lett. **1**, 251 (1962).
[2]A. Barone and G. Paterno, *Physics and Applications of the Josephson Effect* (Wiley, New York, 1982).
[3]K. K. Likharev, *Dynamics of Josephson Junctions and Circuits* (Gordon and Breach, New York, 1986).
[4]J. Bosch, R. Gross, M. Koyanagi, and R. P. Huebener, Phys. Rev. Lett. **54**, 1448 (1985).
[5]J. Mannhart, J. Bosch, R. Gross, and R. P. Huebener, Phys. Rev. B **35**, 5267 (1987); Phys. Lett. A **121**, 241 (1987).
[6]J. Mannhart, J. Bosch, R. Gross, and R. P. Huebener, J. Low. Temp. Phys. **70**, 459 (1988).
[7]J. R. Lhota, M. Scheuermann, P. K. Kuo, and J. T. Chen, Appl. Phys. Lett. **44**, 255 (1983).
[8]B. Mayer, T. Doderer, R. P. Huebener, and A. V. Ustinov, Phys. Rev. B **44**, 12 463 (1991).
[9]S. Meepagala, J. T. Chen, and J.-J. Chang, Phys. Rev. B **36**, 809 (1987).
[10]D. W. McLaughlin and A. C. Scott, Phys. Rev. A **18**, 1652 (1978).
[11]T. Doderer, D. Hoffmann, R. P. Huebener, N. Kirchmann, C. A. Krulle, S. Lachenmann, D. Quenter, J. Schmidt, S. Stehle, J. Niemeyer, R. Poepel, S. P. Benz, and P. A. A. Booi, IEEE Trans. Applied Supercond. (to be published).
[12]K. Takanaka, Solid State Commun. **29**, 443 (1979).
[13]I. O. Kulik, Pis'ma Zh. Eksp. Teor. Fiz. **2**, 134 (1965) [JETP Lett. **2**, 84 (1965)].
[14]K. Enpuku, K. Yoshida, and F. Irie, J. Appl. Phys. **52**, 344 (1981).
[15]R. P. Huebener, in *Advances in Electronics and Electron Physics,* edited by P. W. Hawkes (Academic, New York, 1988), Vol. 70, p. 1.
[16]R. P. Huebener, in *Superconducting Quantum Electronics,* edited by V. Kose (Springer, Berlin, 1989), p. 205.
[17]T. Doderer, D. Quenter, B. Mayer, C. A. Krulle, A. V. Ustinov, and R. P. Huebener, in *Nonlinear Superconductive Electronics and Josephson Devices,* edited by N. F. Pedersen, M. Russo, A. Davidson, G. Costabile, and S. Pagano (Plenum, New York, 1991), p. 353.
[18]T. Doderer, R. P. Huebener, C. A. Krulle, B. Mayer, J. Niemeyer, R. Poepel, and D. Quenter, in *Superconducting Devices and Their Applications,* edited by H. Koch and H. Lübbig, Springer Proceedings in Physics Vol. 64 (Springer, Berlin, 1992), p. 419.
[19]M. P. Soerensen, Ph.D. thesis, Technical University of Denmark, 1984.
[20]E. Turlot, D. Esteve, C. Urbina, M. Devoret, R. Grauer, J. C. Fernandez, H. Politano, and G. Reinisch, Phys. Rev. B **42**, 8418 (1990).
[21]A. H. Nerenberg, P. A. Forsyth, and J. A. Blackburn, J. Appl. Phys. **47**, 4148 (1976).
[22]T. A. Fulton and R. C. Dynes, Solid State Commun. **12**, 57 (1973).
[23]J. J. Chang and J. T. Chen, Phys. Rev. B **22**, 2392 (1980).
[24]J.-J. Chang, Appl. Phys. Lett. **47**, 431 (1985).
[25]O. H. Olsen, N. F. Pedersen, M. R. Samuelsen, H. Svensmark, and D. Welner, Phys. Rev. B **33**, 168 (1986).
[26]S. G. Lachenmann and T. Doderer (unpublished).
[27]N. F. Pedersen, M. R. Samuelsen, and D. Welner, Phys. Rev. B **30**, 4057 (1984).
[28]P. S. Lomdahl, O. H. Soerensen, and P. L. Christiansen, Phys. Rev. B **25**, 5737 (1982).
[29]B. Dueholm, O. A. Levring, J. Mygind, N. F. Pedersen, O. H. Sorensen, and M. Cirillo, Phys. Rev. Lett. **46**, 1299 (1981).
[30]A. V. Ustinov, T. Doderer, R. P. Huebener, N. F. Pedersen, B. Mayer, and V. A. Oboznov, Phys. Rev. Lett. **69**, 1815 (1992).
[31]J. Nagatsuma, K. Enpuku, K. Sueoka, K. Yoshida, and F. Irie, J. Appl. Phys. **58**, 441 (1985).